Morphological Tuning of the Plasmon Dispersion Relation in Dielectric-Loaded Nanofiber Waveguides

Till Leißner,[1,*] Christoph Lemke,[1] Jacek Fiutowski,[2] Jörn Willers Radke,[1] Alwin Klick,[1] Luciana Tavares,[2] Jakob Kjelstrup-Hansen,[2] Horst-Günter Rubahn,[2] and Michael Bauer[1]

[1]*IEAP, University of Kiel, Leibnizstrasse 19, 24118 Kiel, Germany*
[2]*NanoSYD, Mads Clausen Institute, University of Southern Denmark, Alsion 2, 6400 Sønderborg, Denmark*
(Received 21 December 2012; published 24 July 2013)

Understanding the impact of lateral mode confinement in plasmonic waveguides is of fundamental interest regarding potential applications in plasmonic devices. The knowledge of the frequency-wave vector dispersion relation provides the full information on electromagnetic field propagation in a waveguide. This Letter reports on the measurement of the real part of the surface plasmon polariton dispersion relation in the near infrared spectral regime for individual nanoscale plasmonic waveguides, which were formed by deposition of *para*-hexaphenylene (*p*-6P) based nanofibers on top of a gold film. A detailed structural characterization of the nanofibers provides accurate information on the dimensions of the investigated waveguides and enables us to quantify the effect of mode confinement by comparison with experimental results from continuous *p*-6P films and calculations based on the effective index method.

Since plasmonic waveguides offer the promising perspective to confine light on a subwavelength scale they are considered as essential subunits in highly integrated nanoscale optoplasmonic devices. In future applications, there will be a need for custom-designed plasmonic waveguides providing surface plasmon polariton (SPP) propagation parameters adjusted to specific demands [1–3]. High flexibility regarding production and material compatibility of the waveguide for the integration into the device is another prerequisite. Different plasmonic waveguiding schemes have been proposed and successfully realized in the recent past. Examples include metal nanostructures [4–6] and dielectric ridges on top of a metal surface [7–10]. The latter hybrid configuration is often referred to as a dielectric-loaded SPP waveguide (DLSPPW) [11]. The combination of lateral mode confinement and dielectric response of the ridge in DLSPPWs has a strong impact on the specific propagation properties characteristic for the supported plasmonic modes potentially offering the demanded high flexibility for a waveguide design [11–14]. It is therefore of fundamental interest to experimentally provide data on how confinement and material effects modify SPP propagation in plasmonic waveguides and to compare these results with existing analytic and numerical models [15]. The most comprehensive information on plasmonic propagation is in general provided by knowledge of the frequency–wave vector dispersion relation, which has been, for instance, investigated experimentally for nanowire arrays [13] and theoretically for metallic nanowires [16] and *V*-groove structures [17].

Single-crystalline organic nanofibers fabricated by means of self-assembly [18] constitute an attractive and high-potential dielectric component for the construction of DLSPPWs. Recently it was shown that *para*-hexaphenylene (*p*-6P) nanofibers on gold surfaces can support SPP waveguiding in the optical frequency regime [19,20]. Propagation lengths of up to several tens of micrometers were observed experimentally [19] and part of the SPP dispersion relation for a single *p*-6P nanofiber was measured in the excitation wavelengths regime between 720 and 850 nm [20]. Notably, the dimensions, shape, and permittivity of these nanofibers depend critically on the chosen material and self-assembly process parameters [14,21–23], and they therefore offer an exceptional ability for tuning the plasmonic waveguiding properties. This is complemented by further, application-relevant properties reported in the past, including optical waveguiding up to wavelengths in the near ultraviolet [24], a considerable nonlinear optical second-order susceptibility [25], and even the capability to support lasing [26].

In this Letter we report on the measurement and analysis of the real part of the SPP dispersion relation of one-dimensional plasmonic waveguiding at the interface between *p*-6P nanofibers and a gold substrate in the near infrared spectral regime. Application of the two-photon photoemission electron microscopy (2P-PEEM) technique [27–29] enables us to perform dispersion measurements on individual waveguides which were structurally characterized by means of scanning electron microscopy (SEM) and atomic force microscopy (AFM). This comprehensive experimental approach provides the relevant information for a meaningful comparison of the dispersion data with calculations based on the effective index method (EIM) [11]. It allows us to unambiguously assign the differences in the dispersion relation observed for different nanofibers to nanofiber-to-nanofiber structural variations in the cross-sectional dimensions.

The investigated nanofibers were grown by molecular beam epitaxy on a freshly cleaved and heated mica substrate. DLSPPWs were formed by transfer of the fibers via a roll-printing technique onto 100 nm thick gold films deposited on a silicon substrate [12,30]. The shape and size of the deposited nanofibers were characterized after the photoemission electron microscopy (PEEM) experiments by AFM (Dimension 3100 AFM, Veeco) and SEM (S-4800, Hitachi). Dispersion relation measurements were conducted using a photoemission electron microscope (IS PEEM, Focus GmbH) [31] mounted in an ultrahigh vacuum μ-metal chamber. The sample was excited by 100 fs laser pulses from a Ti:sapphire oscillator (Tsunami, Spectra Physics). The central wavelength of this laser system is continuously tunable from 710 to 890 nm and was measured using a calibrated fiber optic spectrometer right in front of the fused silica entrance window into the ultrahigh vacuum chamber.

Figure 1(a) shows an atomic force micrograph of an individual p-6P nanofiber supported by a gold film. The overall length of the fiber is 24 μm. A cross-sectional analysis reveals a fiber height of 20 nm. The cross section of the fiber (in the following referred to as fiber 1) along the dashed line in Fig. 1(a) is shown in Fig. 1(e) in comparison to the cross section of two other fibers (fiber 2 and fiber 3) on the sample. SEM images are used to accurately determine the width of the investigated nanofibers. A SEM image of fiber 1 is shown in Fig. 1(b). The quantitative analysis yields a width of 900 nm. Both AFM and SEM data show some imperfections in the fiber morphology which can mainly be ascribed to the manual mica-gold transfer process. As-deposited fibers on mica feature much less distortion [24]. Overall, variations in height and width were less than 10%. Relevant structural data of all three fibers are summarized in Table I.
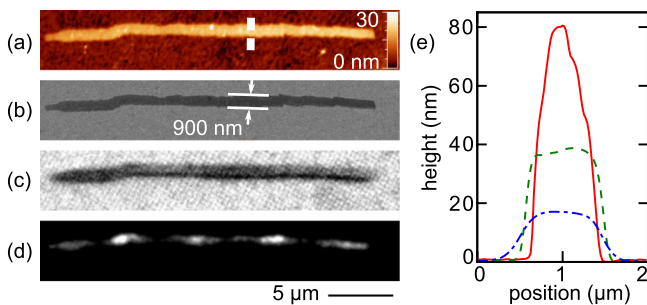
Finally, Figs. 1(c) and 1(d) compare PEEM images of fiber 1 recorded in conventional threshold mode (illumination at $h\nu = 4.9$ eV) and in 2P-PEEM mode ($h\nu = 1.55$ eV), respectively. At excitation with 1.55 eV photons a periodic intensity pattern localized at the nanofiber is observed, which indicates one-dimensional SPP propagation along the fiber [19]. The pattern is completely absent in Fig. 1(c) as 4.9 eV photons cannot couple to any SPP mode at a gold interface [12,32]. Note, furthermore, that also in the AFM and the SEM images no obvious indications for a periodic pattern are observed. Furthermore, none of the three nanofibers exhibits breaks as reported, e.g., in Ref. [33]. However, some irregularities in the morphology of the fibers are visible in the AFM and the SEM images, which may result in a locally enhanced nonlinear photoemission yield. Such "hot spots" have to be considered carefully within the analysis of the 2P-PEEM data (see the Supplemental Material [34]).

The periodic 2P-PEEM pattern results from the phase-coupled superposition of the polarization field of the propagating SPP and the excitation laser field [35]. The actual signature that is imaged is the wave vector mismatch Δk between the SPP and the laser field

$$\Delta k = k_{\text{beat}} = k'_{\text{SPP}} - k_{\text{Laser}}, \tag{1}$$

which results in a beating pattern of the superposition field at a wavelength $\lambda_{\text{beat}} = 2\pi/\Delta k$. Here, k'_{SPP} is the real part of the complex SPP wave vector $k_{\text{SPP}} = k'_{\text{SPP}} + ik''_{\text{SPP}}$ and k_{Laser} is the wave vector of the laser.

Under consideration of Eq. (1) and for a known laser wavelength $\lambda_{\text{Laser}} = 2\pi/k_{\text{Laser}}$, measurement of λ_{beat} allows us to determine the SPP wave vector k'_{SPP}. With the frequency ω_{SPP} of the SPP given by the laser excitation frequency $\omega_{\text{Laser}} = ck_{\text{Laser}}$, where c is the vacuum speed of light, we finally gain access to the SPP dispersion relation. Experimentally, it only remains to measure the beating pattern wavelength λ_{beat} as a function of the excitation wavelength λ_{Laser}.

In the following we will present corresponding 2P-PEEM results for fibers 1, 2, and 3. Figures 2(a)–2(d) compare 2P-PEEM images of fiber 1 recorded at illumination at different central laser wavelengths ranging between 728 and 872 nm. The laser beam is incident from the left. Marked by the gray guiding lines, a clear change in the beating pattern period is observed. The overall variation ranges from $\lambda_{\text{beat}} = 4.24$ μm at excitation with $\lambda_{\text{Laser}} = 728$ nm to $\lambda_{\text{beat}} = 6.27$ μm at $\lambda_{\text{Laser}} = 872$ nm. According to Eq. (1), the shift arises from changes in the wave vector

FIG. 1 (color online).   Characterization of a p-6P nanofiber by complementary microscopy techniques: (a) atomic force micrograph of a single p-6P nanofiber (fiber 1) on top of a 100 nm thick gold film (composed of six AFM scans); (b) the same nanofiber mapped by SEM; (c),(d) fiber 1 as imaged by threshold PEEM ($h\nu = 4.9$ eV) and 2P-PEEM ($h\nu = 1.55$ eV, laser incident from the left); (e) cross-sectional shapes of three different nanofibers from AFM measurements: fiber 1 (dotted dashed line), fiber 2 (dashed line), fiber 3 (solid line). The dashed line in (a) indicates the position of the displayed cross section of fiber 1.

TABLE I.   Cross-sectional dimensions of fibers 1, 2, and 3.

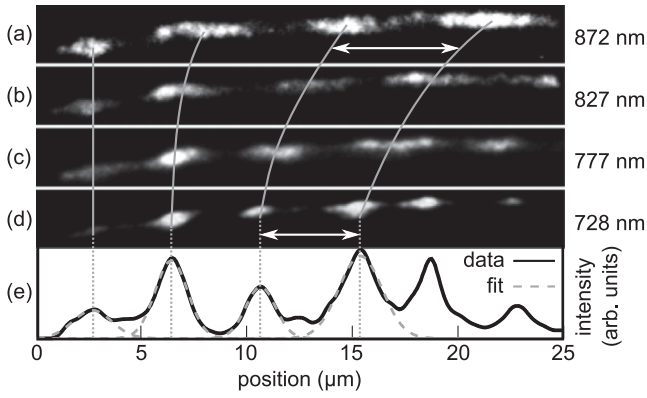|	Width (nm)	Height (nm)	$\sigma = \frac{\text{height}}{\text{width}}$
Fiber 1	900	20	0.02
Fiber 2	700	35	0.05
Fiber 3	450	75	0.17

FIG. 2.   Fiber 1 imaged in 2P-PEEM mode at varying excitation wavelengths λ_{Laser}: (a) 872 nm, (b) 827 nm, (c) 777 nm, and (d) 728 nm. The gray lines indicate the position of the observed beating pattern maxima. (e) Intensity profile along the nanofiber for $\lambda_{\text{Laser}} = 728$ nm (solid line) including a fit to the beating pattern maxima (dashed line).
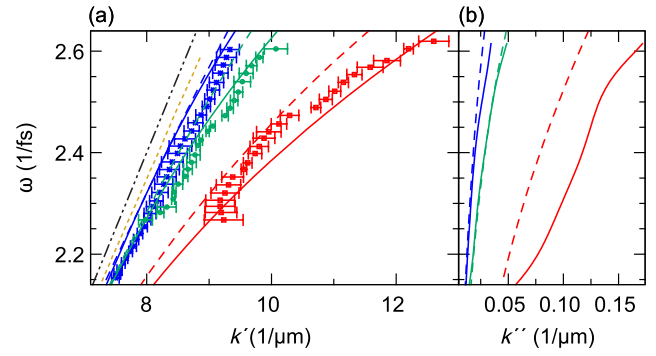

FIG. 3 (color online). Experimental SPP dispersion curves of fiber 1 (asterisk), 2 (circled dot) and 3 (squared dot). (a) Comparison to different effective index calculations (dashed and solid lines, see text for further information); the dash-dotted line is the dispersion line of light $\omega = ck$. The short dashed line is an experimental SPP dispersion curve of a gold-vacuum interface. (b) Calculated imaginary part of the SPP dispersion relation [dashed and solid lines corresponding to (a)].

mismatch between the laser and the SPP and can, therefore, directly be assigned to the dispersing character of the excited SPP mode. For the quantitative evaluation of the data we fit the individual beating pattern maxima profiles by single Gaussians, as illustrated in Fig. 2(e) for the 2P-PEEM image shown in Fig. 2(d). The maxima positions of the Gaussians are then used to determine the actual beating pattern wavelength λ_{beat} and subsequently the SPP wave vector k'_{SPP} [see Eq. (1)]. Overall, such an analysis was applied to experimental data from fiber 1, fiber 2, and fiber 3 recorded in an excitation wavelength regime between 710 and 890 nm at a step size of 5 nm. To eliminate some distorting contributions from small-sized defect structures, a high-pass filter was applied to every PEEM image prior to the quantitative analysis. Assignment of k'_{SPP} to the respective laser excitation frequencies finally yields the real part of the SPP dispersion relation for each nanofiber in the experimentally probed wave vector regime.

The results of the quantitative analysis of the three nanofibers are compared in Fig. 3(a). The error bars of the experimental dispersion curves correspond to the variance in the determination of λ_{beat}. In comparison to a gold-vacuum interface (short dashed line), the nanofibers show a clear shift of the SPP dispersion relation to higher wave vectors. This shift results from the dielectric load of the gold surface by the material of the nanofiber as well as the lateral confinement of the plasmonic mode governed by the nanofiber geometry.

We observe furthermore a very significant difference in the dispersion relation between the individual nanofibers. Whereas, for instance, fiber 1 shows a steep slope rather close to the data of the gold-vacuum SPP and also a fairly linear dispersion in the probed frequency regime, the dispersion of fiber 3 is considerably flattened and exhibits a clear curvature. These differences can be assigned to the

differences in the cross-sectional dimension of the individual p-6P nanofibers, as will be discussed in the following.

To gain a more quantitative understanding of the geometrical constraints set by the fiber cross section on the SPP dispersion relation, we performed simulations based on the effective index method (EIM) [11]. Here the two-dimensional problem as defined by the waveguide cross section is split up into two separate one-dimensional problems, which can be solved subsequently using common multilayer mode solvers. The adaptability of this simulation procedure to the description of the plasmonic response of deposited p-6P nanofibers was verified in a recent work by Radko *et al.* [20]. In Fig. 3(a) we compare the results of our simulations (dashed and solid lines), performed under consideration of the actual fiber geometries as determined in the AFM and SEM measurements (see Table I), with the experimental dispersion curves. The dashed lines represent full effective index calculations where both steps of the simulation [(i) the effective index calculation of a homogenous p-6P film for a thickness given by the fiber height and (ii) the effective index calculation of the confinement by the fiber width] were executed. The optical properties of gold used in the calculations were taken from Ref. [36]. For p-6P and the Si substrate constant indices of refraction of $n_{p\text{-}6P} = 1.7$ [37] and $n_{\text{Si}} = 3.7$ [38] were used, respectively. In contrast, the solid lines represent calculations where the first step of the effective index method was replaced by the experimental results for homogeneous p-6P films of varying film thickness ranging from 22 to 88 nm on top of a gold substrate [39]. In the following the different calculations will be referred to as EIM$_{\text{sim}}$ and EIM$_{\text{film}}$, respectively.

Both absolute values as well as the overall shape of the experimental dispersion curves are already well reproduced by the EIM$_{\text{sim}}$ simulation approach for all three

TABLE II.　SPP phase and group velocities at $\omega = 2.36$ fs^{-1} in units of c compared to effective index simulation results.

	PEEM v_{ph} (c)	PEEM v_g (c)	EIM$_{sim}$ v_g (c)	EIM$_{film}$ v_g (c)
Fiber 1	0.94 ± 0.01	0.79 ± 0.01	0.85	0.79
Fiber 2	0.91 ± 0.01	0.65 ± 0.03	0.75	0.66
Fiber 3	0.84 ± 0.01	0.32 ± 0.04	0.47	0.33

FIG. 4 (color online).　The electric field distributions $|E_z|$ of the fundamental SPP modes.

fibers with some indication for a slight and systematic underestimation of the dispersion curve wave number. This agreement is further improved at comparison with EIM$_{film}$, in particular for the case of fibers 2 and 3. We suspect that this improvement results from the actual permittivity of p-6P thin films and p-6P nanofibers being different from the permittivity of bulk p-6P samples, a quantity which was used as input for the EIM$_{sim}$ calculations [40].

Knowledge of the real part of the dispersion relation gives us direct access to relevant SPP propagation parameters of the waveguide such as the SPP phase velocity $v_{ph,SPP} = \omega/k'$ and the SPP group velocity $v_{g,SPP} = d\omega/dk'$. The high resolution microscopy approach applied in this work enables us to determine these quantities for individual, well selected nanoscale plasmonic waveguides. For illustration, Table II compares SPP velocity data for the three nanofibers deduced from the experiment ($v_{ph,SPP}$ and $v_{g,SPP}$) and the simulations ($v_{g,SPP}$) for a selected plasmon frequency ($\omega = 2.36$ fs^{-1}). As expected from the comparison of the dispersion curves, experiment and EIM calculations show very similar results and a particularly good agreement between experiment and EIM$_{film}$ calculations.

The group and phase velocity of an SPP waveguiding mode can also be determined in a time-domain experiment by means of the ITR-PEEM technique [19,35]. We performed such a measurement to verify the predicted rather slow propagation of an SPP wave packet along the interface between fiber 3 and the gold surface (see the Supplemental Material [34]). The quantitative analysis of the real-time study yields a group velocity $v_{g,SPP} = (0.26 \pm 0.02)c$ for SPP propagation, supporting our findings of the frequency domain study in a satisfactory manner.

The fundamental origin of the dispersion is related to both the frequency-dependent optical properties of the gold substrate and to the nanofiber geometry, which determines the degree of mode confinement within the fibers [11]. As the widths of the fibers investigated in the present work are in the range of the wavelength or even smaller only a weak mode confinement can be achieved. The strong dispersive character of the SPP must be ascribed therefore mainly to the nanofiber dimensions rather than to the optical properties of the gold. An exception is fiber 3. Figure 4 shows the electric field distributions $|E_z|$ of the fundamental SPP
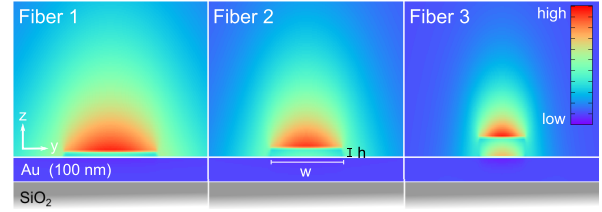
modes of the three fiber geometries as calculated within the framework of the finite-element method [11,41]. The main part of the electric field distribution for the investigated fiber heights is located above the nanofibers. Only for fiber 3 is a substantial fraction of the electric field also located at the p-6P-gold interface.

Besides the real part of the SPP dispersion relation k'_{SPP}, the imaginary part k''_{SPP} and the SPP propagation length $L = 1/(2k''_{SPP})$, respectively, can also be calculated within the framework of the effective index method. SPP damping arises from Ohmic losses in the gold substrate and coupling to the radiation field mediated, for instance, by the presence of defects in the nanofiber. Another damping channel might be provided by coupling to SPP modes propagating along the gold-vacuum interface. Calculated k''_{SPP} dispersion curves for the three nanofiber geometries are shown in Fig. 3(b). As for k'_{SPP}, EIM$_{sim}$ (dashed lines) and EIM$_{film}$ (solid lines) calculations were performed. The experimental input for the EIM$_{film}$ calculations are 2P-PEEM data of k''_{SPP} for homogeneous p-6P films [39]. The general trend is an increase of k''_{SPP} and a decrease of the propagation length L, respectively, with increasing nanofiber height. At a frequency $\omega = 2.36$ fs^{-1}, the k''_{SPP} curves (EIM$_{film}$) yield propagation lengths $L \approx 28\,\mu$m for fiber 1, $L \approx 19\,\mu$m for fiber 2, and $L \approx 5\,\mu$m for fiber 3. This trend is corroborated by the simulations of the SPP field distribution for the three fiber geometries (see Fig. 4). The electric field located at the gold-fiber interface in the case of fiber 3 will affect the SPP propagation length.

In summary, we presented in this Letter a combined PEEM-AFM-SEM study on one-dimensional plasmonic waveguiding supported by p-6P nanofibers deposited on a gold surface. The comprehensive experimental approach in combination with effective index simulations enabled us to determine the SPP dispersion relation of individual plasmonic waveguides and to directly relate the dispersion properties to structural characteristics of the p-6P nanofibers. The flexibility and ease at which p-6P nanofibers can be structurally manipulated by defined adjustment of the growth parameters offers a means to provide plasmonic waveguides with dedicated properties on demand. By improving the transfer process of the nanofibers from mica to gold, e.g., by proper controlling of the contact pressure, the homogeneity of the fibers will probably be increased considerably in the future. We finally would like

to emphasize that this study substantially relied on the capability of the PEEM technique to monitor plasmonic excitations on nanoscale dimensions [27,35,42–44]. The measurement of dispersion curves of individual nanosized objects using 2P-PEEM adds a new and very promising aspect to the versatile capabilities of this technique in characterizing plasmonic systems.

---

*leissner@physik.uni-kiel.de

[1] W. L. Barnes, A. Dereux, and T. W. Ebbesen, Nature (London) **424**, 824 (2003).

[2] D. K. Gramotnev and S. I. Bozhevolnyi, Nat. Photonics **4**, 83 (2010).

[3] E. Ozbay, Science **311**, 189 (2006).

[4] A. L. Pyayt, B. Wiley, Y. Xia, A. Chen, and L. Dalton, Nat. Nanotechnol. **3**, 660 (2008).

[5] M. Ohtsu, K. Kobayashi, T. Kawazoe, S. Sangu, and T. Yatsui, IEEE J. Sel. Top. Quantum Electron. **8**, 839 (2002).

[6] S. I. Bozhevolnyi, V. S. Volkov, E. Devaux, J.-Y. Laluet, and T. W. Ebbesen, Nature (London) **440**, 508 (2006).

[7] J. Grandidier, S. Massenot, G. C. desFrancs, A. Bouhelier, J.-C. Weeber, L. Markey, A. Dereux, J. Renger, M. U. González, and R. Quidant, Phys. Rev. B **78**, 245419 (2008).

[8] N.-N. Feng, M. L. Brongersma, and L. Dal Negro, IEEE J. Quantum Electron. **43**, 479 (2007).

[9] J. Gosciniak, T. Holmgaard, and S. I. Bozhevolnyi, J. Lightwave Technol. **29**, 1473 (2011).

[10] A. V. Krasavin and A. V. Zayats, Phys. Rev. B **78**, 045425 (2008).

[11] T. Holmgaard and S. I. Bozhevolnyi, Phys. Rev. B **75**, 245405 (2007).

[12] T. Leißner, K. Thilsing-Hansen, C. Lemke, S. Jauernik, J. Kjelstrup-Hansen, M. Bauer, and H.-G. Rubahn, Plasmonics **7**, 253 (2012).

[13] G. Schider, J. R. Krenn, A. Hohenau, H. Ditlbacher, A. Leitner, F. R. Aussenegg, W. L. Schaich, I. Puscasu, B. Monacelli, and G. Boreman, Phys. Rev. B **68**, 155427 (2003).

[14] T. Holmgaard, Z. Chen, S. I. I. Bozhevolnyi, A. Dereux, N. B. All, and L. Markey, Opt. Express **17**, 2968 (2009).

[15] R. F. Oulton, V. J. Sorger, D. A. Genov, D. F. P. Pile, and X. Zhang, Nat. Photonics **2**, 496 (2008).

[16] U. Schröter and A. Dereux, Phys. Rev. B **64**, 125420 (2001).

[17] V. A. Zenin, V. S. Volkov, Z. Han, S. I. Bozhevolnyi, E. Devaux, and T. W. Ebbesen, J. Opt. Soc. Am. B **28**, 1596 (2011).

[18] L. Kankate, F. Balzer, H. Niehus, and H.-G. Rubahn, J. Chem. Phys. **128**, 084709 (2008).

[19] T. Leißner, C. Lemke, S. Jauernik, M. Müller, J. Fiutowski, J. Kjelstrup-Hansen, O. Magnussen, H.-G. Rubahn, and M. Bauer, Opt. Express **21**, 8251 (2013).

[20] I. P. Radko, J. Fiutowski, L. Tavares, H.-G. Rubahn, and S. I. Bozhevolnyi, Opt. Express **19**, 15155 (2011).

[21] F. Balzer, L. Kankate, H. Niehus, R. Frese, C. Maibohm, and H.-G. Rubahn, Nanotechnology **17**, 984 (2006).

[22] M. Schiek, F. Balzer, K. Al-Shamery, A. Lützen, and H.-G. Rubahn, Soft Matter **4**, 277 (2008).

[23] F. Balzer, J. Beermann, S. I. Bozhevolnyi, A. C. Simonsen, and H.-G. Rubahn, Nano Lett. **3**, 1311 (2003).

[24] F. Balzer, V. G. Bordo, A. C. Simonsen, and H.-G. Rubahn, Appl. Phys. Lett. **82**, 10 (2003).

[25] J. Beermann, S. I. Bozhevolnyi, V. G. Bordo, and H.-G. Rubahn, Opt. Commun. **237**, 423 (2004).

[26] F. Quochi, F. Cordella, R. Orru, J. E. Communal, P. Verzeroli, A. Mura, G. Bongiovanni, A. Andreev, H. Sitter, and N. S. Sariciftci, Appl. Phys. Lett. **84**, 4454 (2004).

[27] L. Douillard, F. Charra, Z. Korczak, R. Bachelot, S. Kostcheev, G. Lerondel, P.-M. Adam, and P. Royer, Nano Lett. **8**, 935 (2008).

[28] O. Schmidt, M. Bauer, C. Wiemann, R. Porath, M. Scharte, O. Andreyev, G. Schönhense, and M. Aeschlimann, Appl. Phys. B **74**, 223 (2002).

[29] M. Cinchetti, A. Gloskovskii, S. A. Nepjiko, G. Schonhense, H. Rochholz, and M. Kreiter, Phys. Rev. Lett. **95**, 047601 (2005).

[30] L. Tavares, J. Kjelstrup-Hansen, and H.-G. Rubahn, Small **7**, 2460 (2011).

[31] W. Swiech, G. Fecher, C. Ziethen, O. Schmidt, G. Schönhense, K. Grzelakowski, C. M. Schneider, R. Frömter, H. Oepen, and J. Kirschner, J. Electron Spectrosc. Relat. Phenom. **84**, 171 (1997).

[32] W. A. Murray and W. L. Barnes, Adv. Mater. **19**, 3771 (2007).

[33] F. Balzer, V. G. Bordo, A. C. Simonsen, and H.-G. Rubahn, Phys. Rev. B **67**, 115408 (2003).

[34] See Supplemental Material at http://link.aps.org/supplemental/10.1103/PhysRevLett.111.046802 for information on data analysis and ITR-PEEM results.

[35] A. Kubo, N. Pontius, and H. Petek, Nano Lett. **7**, 470 (2007).

[36] P. B. Johnson and R. W. Christy, Phys. Rev. B **6**, 4370 (1972).

[37] A. Niko, S. Tasch, F. Meghdadi, C. Brandstätter, and G. Leising, J. Appl. Phys. **82**, 4177 (1997).

[38] *Handbook of Optical Constants of Solids*, edited by E. D. Palik (Academic Press Inc, New York, 1985), 1st ed.

[39] C. Lemke, T. Leißner, A. Klick, J. Fiutowski, J. W. Radke, J. Kjelstrup-Hansen, H.-G. Rubahn, and M. Bauer (to be published).

[40] V. G. Bordo, Phys. Rev. B **73**, 205117 (2006).

[41] O. C. Zienkiewicz, R. L. Taylor, and J. Z. Zhu, *The Finite Element Method: Its Basis and Fundamentals* (Butterworth Heinemann, Oxford, 2005), 6th ed., p. 752.

[42] M. Bauer, C. Wiemann, J. Lange, D. Bayer, M. Rohmer, and M. Aeschlimann, Appl. Phys. A **88**, 473 (2007).

[43] C. Lemke, T. Leißner, S. Jauernik, A. Klick, J. Fiutowski, J. Kjelstrup-Hansen, H.-G. Rubahn, and M. Bauer, Opt. Express **20**, 12877 (2012).

[44] F.-J. Meyer zu Heringdorf, L. Chelaru, S. Möllenbeck, D. Thien, and M. Horn-von Hoegen, Surf. Sci. **601**, 4700 (2007).